

# Measuring stellar magnetic helicity density

K. Lund<sup>1</sup>,<sup>\*</sup> M. Jardine<sup>1</sup>, L. T. Lehmann,<sup>1</sup> D. H. Mackay,<sup>2</sup> V. See,<sup>3</sup> A. A. Vidotto<sup>4</sup>,  
J.-F. Donati,<sup>5</sup> R. Fares,<sup>6</sup> C. P. Folsom,<sup>5</sup> S. V. Jeffers,<sup>7</sup> S. C. Marsden,<sup>8</sup> J. Morin<sup>9</sup>  
and P. Petit<sup>5</sup>

<sup>1</sup>*SUPA, School of Physics and Astronomy, University of St Andrews, North Haugh, St Andrews KY16 9SS, UK*

<sup>2</sup>*School of Mathematics and Statistics, University of St Andrews, North Haugh, St Andrews KY16 9SS, UK*

<sup>3</sup>*University of Exeter, Department of Physics & Astronomy, Stocker Road, Devon, Exeter EX4 4QL, UK*

<sup>4</sup>*School of Physics, Trinity College Dublin, the University of Dublin, College Green, Dublin-2, Ireland*

<sup>5</sup>*IRAP, Université de Toulouse, CNRS, UPS, CNES, 14 Avenue Edouard Belin, F-31400 Toulouse, France*

<sup>6</sup>*Physics Department, United Arab Emirates University, PO Box 15551, Al-Ain, United Arab Emirates*

<sup>7</sup>*Institut für Astrophysik, Universität Göttingen, Friedrich-Hund-Platz 1, D-37077 Göttingen, Germany*

<sup>8</sup>*University of Southern Queensland, Centre for Astrophysics, Toowoomba QLD 4350, Australia*

<sup>9</sup>*LUPM, Université de Montpellier, CNRS, Place Eugène Bataillon, F-34095 Montpellier, France*

Accepted 2020 January 28. Received 2020 January 28; in original form 2019 December 13

## ABSTRACT

Helicity is a fundamental property of a magnetic field but to date it has only been possible to observe its evolution in one star – the Sun. In this paper, we provide a simple technique for mapping the large-scale helicity density across the surface of any star using only observable quantities: the poloidal and toroidal magnetic field components (which can be determined from Zeeman–Doppler imaging) and the stellar radius. We use a sample of 51 stars across a mass range of 0.1–1.34  $M_{\odot}$  to show how the helicity density relates to stellar mass, Rossby number, magnetic energy, and age. We find that the large-scale helicity density increases with decreasing Rossby number  $R_o$ , peaking at  $R_o \simeq 0.1$ , with a saturation or decrease below that. For both fully and partially convective stars, we find that the mean absolute helicity density scales with the mean squared toroidal magnetic flux density according to the power law:  $|\langle h \rangle| \propto \langle B_{\text{tor}}^2 \rangle^{0.86 \pm 0.04}$ . The scatter in this relation is consistent with the variation across a solar cycle, which we compute using simulations and observations across solar cycles 23 and 24, respectively. We find a significant decrease in helicity density with age.

**Key words:** methods: analytical – stars: magnetic field – Sun: magnetic fields.

## 1 INTRODUCTION

The helicity of a magnetic field is one of its most powerful measures. As an invariant of the ideal MHD equations (Woltjer 1958; Taylor 1974), it is a fundamental ingredient in our understanding of magnetic field generation and evolution. It relates the large and small scales within a magnetic field and constrains the evolution of that field towards a lowest energy state. Helicity that has been captured by stars during their formation may be enhanced by the stellar dynamo and returned to the interstellar medium by the action of stellar winds and ejecta (Berger & Ruzmaikin 2000; Zhang & Low 2005; Zhang 2013; Blackman 2015).

Measuring the helicity ( $H$ ) of an astronomical magnetic field is, however, extremely challenging, as it is inherently a three-dimensional (3D) quantity that measures the linkage of fields. It can be defined in terms of the vector potential ( $\mathbf{A}$ ) and the corresponding

magnetic field ( $\mathbf{B} = \nabla \times \mathbf{A}$ ) as (Woltjer 1958)

$$H = \int \mathbf{A} \cdot \mathbf{B} dV, \quad (1)$$

where  $V$  is volume. This reveals one of the challenges inherent in determining helicity – that it is defined only for a given gauge. The transformation  $\mathbf{A} \rightarrow \mathbf{A} + \nabla\psi$  gives the same magnetic field  $\mathbf{B}$  but a different helicity. This problem is resolved in a closed magnetic volume where the helicity is well defined, but if some flux penetrates the boundary, we can only define the helicity relative to a given field, normally chosen to be the potential field with the same boundary flux (Berger & Field 1984).

To date helicity has been measured for the Sun, but not other stars. There are many areas of current solar research where helicity plays a significant role and thus we limit our discussion to a few examples of its application. Magnetic helicity is central to the understanding of the evolution and generation of magnetic fields, i.e. solar dynamo theory (Brandenburg & Subramanian 2005; Chatterjee, Guerrero & Brandenburg 2011), as well as to characterizing the topology of

\* E-mail: [kblg@st-andrews.ac.uk](mailto:kblg@st-andrews.ac.uk)

coronal magnetic fields (Berger & Field 1984). Active regions on the Sun, where the magnetic fields are especially strong, frequently give rise to explosive events such as solar flares and coronal mass ejections (CMEs). Rust (1994) proposed CMEs are a direct result of the conservation of helicity, necessary in order to remove excess helicity from the Sun. Subsequently, helicity has been studied extensively as a diagnostic of solar eruptivity (Zhang, Flyer & Low 2006; Zhang & Flyer 2008; Zhang, Flyer & Chye Low 2012; Nindos 2013). Attempting to improve space weather predictions Pariat et al. (2017) linked the build-up of magnetic helicity to the likelihood of a solar eruption, and Hawkes & Berger (2018) used helicity flux to predict overall solar activity. Studies such as these have motivated numerous authors to attempt measurements of magnetic helicity in the solar atmosphere [see reviews by Démoulin (2007) and Démoulin & Pariat (2009)].

Magnetic helicity in stellar research is not as well studied. Most recently, Warnecke & Peter (2019) have modelled the impact of helicity on stellar X-ray emission, suggesting that the rise in X-ray emission with increasing rotation rate may be related to the underlying variation in the helicity.

In this paper, we use observations of magnetic fields at stellar surfaces to extend the study of helicity from the Sun to a large sample of stars. Mapping magnetic fields across stellar surfaces has been made possible by the Zeeman–Doppler Imaging (ZDI) technique (Semel 1989) that has now been applied to a large range of stars (see e.g. Donati & Landstreet 2009). Many surveys, such as MagIcS,<sup>1</sup> Bcool,<sup>2</sup> MaTYSSSE,<sup>3</sup> Toupies<sup>4</sup> and MaPP,<sup>5</sup> have explored magnetic field behaviour in a range of stars. One of the most intriguing early results was that for stars of similar mass to the Sun, field geometries are largely toroidal below Rossby number  $R_o \approx 1$  (Donati & Landstreet 2009), prompting interest in exploring dynamo models that allow for strong surface toroidal fields (Bonanno 2016).

The ratio of toroidal-to-poloidal magnetic energies is well recovered by ZDI (Lehmann et al. 2019) and appears to be different for stars that are fully convective and those that are only convective in the outer regions of their interiors (Donati et al. 2008b; Gregory et al. 2012; See et al. 2015). Fully convective stars tend to be those that are either very young, or have low masses. Since they do not possess a tachocline at the interface between an inner radiative and outer convective zones, they cannot support a deep-seated interface dynamo. The nature of dynamo activity (and hence the types of field geometries produced) may therefore be different for these two different types of interior structure. A transition from strong, axisymmetric fields to weaker, more complex fields appears to occur in young stars when the radiative core forms (e.g. Donati et al. 2011; Folsom et al. 2016). Studies of main-sequence M dwarfs also show that for masses below  $\sim 0.5 M_\odot$  there is an apparent transition from weaker, complex fields to stronger, simpler fields (Donati et al. 2008c; Morin et al. 2008b; Donati & Landstreet 2009; Morin et al. 2010). This may be related to a change in the nature of the dynamo across the fully convective boundary.

Berger (1985) and Berger & Hornig (2018) describe in detail how the poloidal–toroidal magnetic field decomposition allows for a simple expression of helicity, as the net linking of toroidal and poloidal fields. This particular field decomposition has the added

advantage of simplifying the treatment of the gauge. Since the corresponding potential field with the same boundary flux is purely poloidal and therefore has zero helicity, calculating the helicity in this decomposition is straightforward. In the context of ZDI maps however, which only provide *surface* magnetic fields, there is not enough information available to calculate magnetic helicities, as this is a property within a *volume*. Consequently, in our work, we consider the surface magnetic helicity density instead.

In a similar way, Pipin et al. (2019) used poloidal and toroidal field components to calculate the evolution of the Sun’s magnetic helicity density across solar cycle 24. They showed the relationship between the small-scale (active region) and large-scale (polar) fields through the solar cycle. According to their results, the large-scale and small-scale helicities started off with opposite signs at the beginning of the solar cycle, and then evolved to show the same sign in the declining phase. Furthermore, they measured the helicity of large-scale fields to be an order of magnitude smaller than the helicity of small-scale fields.

One of the limitations of the ZDI technique is that it is insensitive to small-scale magnetic flux elements whose polarities cancel out (Reiners & Basri 2009; Morin et al. 2010; Kochukhov & Shulyak 2019; See et al. 2019). We are therefore unable to explore the evolution of helicity across a large range of length scales in the way that is possible for the Sun. What we observe is rather the imprint of that helicity evolution on the largest scales. This may improve when moving to nIR data, e.g. using SPIRou, thanks to the larger Zeeman effect. By applying our technique to both observed and simulated solar magnetograms, however, we can place the Sun in the context of other stars and use this to help interpret stellar observations. We can determine the role of different length scales by expressing the poloidal and toroidal magnetic field components ( $\mathbf{B} = \mathbf{B}_{\text{pol}} + \mathbf{B}_{\text{tor}}$ ) as a sum of spherical harmonics of different  $l$  modes, where the smaller  $l$  modes describe the larger-scale field and higher  $l$  modes describe the smaller scale field. Truncating the sum at some maximum  $l$  value mimics the lack of sensitivity to small-scale fields.

In this paper, we provide the reader with a simple equation for helicity density, given the poloidal and toroidal decomposition of any stellar magnetic field. We use this expression to study the large-scale helicity density of 51 stars. Our sample includes both fully and partially convective stars. Our aim is to discover how the helicity of these fields relates to fundamental stellar properties and to interpret these results in the context of the evolution of the large-scale helicity density of the Sun.

The paper is outlined as follows. Section 2 describes the derivation of the magnetic helicity density in terms of poloidal and toroidal magnetic field components. In Section 3, we calculate the helicity density of the Sun, as well as our sample of stars. Section 4 presents our discussion of the results. A summary of our results along with our conclusions are given in Section 5.

## 2 MAGNETIC HELICITY DENSITY

The magnetic helicity density is given by the integrand of equation (1):

$$h = \mathbf{A} \cdot \mathbf{B}. \quad (2)$$

We expand the magnetic field and the vector potential field into their poloidal and toroidal components as follows:

$$h = (\mathbf{A}_{\text{pol}} + \mathbf{A}_{\text{tor}}) \cdot (\mathbf{B}_{\text{tor}} + \mathbf{B}_{\text{pol}}). \quad (3)$$

<sup>1</sup><http://www.ast.obs-mip.fr/users/donati/magics/v1/>

<sup>2</sup>[http://bcool.ast.obs-mip.fr/Bcool/Bcool...cool\\_magnetic\\_stars.html](http://bcool.ast.obs-mip.fr/Bcool/Bcool...cool_magnetic_stars.html)

<sup>3</sup><https://matysse.irap.omp.eu/doku.php>

<sup>4</sup><http://ipag.osug.fr/Anr.Toupies/>

<sup>5</sup><http://cfht.hawaii.edu/Science/MAPP/>

An expression for the magnetic field is derived in Section 2.1, a corresponding vector potential is calculated in Section 2.2, and we combine them to obtain an expression for the helicity density in Section 2.3.

### 2.1 Poloidal and toroidal magnetic field components

We decompose the stellar magnetic field in terms of a poloidal and toroidal component following appendix III of Chandrasekhar (1961):

$$\mathbf{B}_{\text{pol}} = \nabla \times [\nabla \times (\Phi \hat{\mathbf{r}})], \quad (4)$$

$$\mathbf{B}_{\text{tor}} = \nabla \times (\Psi \hat{\mathbf{r}}). \quad (5)$$

In a spherical coordinate system<sup>6</sup> the scalars  $\Phi$  and  $\Psi$  can be written in terms of spherical harmonics as

$$\Phi = S(r) c_{lm} P_{lm} e^{im\phi} \quad (6)$$

and

$$\Psi = T(r) c_{lm} P_{lm} e^{im\phi}. \quad (7)$$

$S(r)$  and  $T(r)$  are functions describing the radial behaviour of the field,  $P_{lm}$  is short for the Legendre Polynomial  $P_{lm}(\cos \theta)$  of mode  $l$  and order  $m$ , and  $c_{lm}$  is the associated normalization constant:

$$c_{lm} = \sqrt{\frac{2l+1}{4\pi} \frac{(l-m)!}{(l+m)!}}. \quad (8)$$

Expanding the poloidal and toroidal field components gives the following expressions:

$$\begin{aligned} \mathbf{B}_{\text{pol}}(r, \theta, \phi) &= \sum_{lm} \frac{l(l+1)}{r^2} S(r) c_{lm} P_{lm} e^{im\phi} \hat{\mathbf{r}} \\ &+ \sum_{lm} \frac{1}{r} \frac{dS(r)}{dr} c_{lm} \frac{dP_{lm}}{d\theta} e^{im\phi} \hat{\boldsymbol{\theta}} \\ &+ \sum_{lm} \frac{im}{r \sin \theta} \frac{dS(r)}{dr} c_{lm} P_{lm} e^{im\phi} \hat{\boldsymbol{\phi}}, \end{aligned} \quad (9)$$

$$\begin{aligned} \mathbf{B}_{\text{tor}}(r, \theta, \phi) &= \sum_{lm} \frac{T(r) im}{r \sin \theta} c_{lm} P_{lm} e^{im\phi} \hat{\boldsymbol{\theta}} \\ &- \sum_{lm} \frac{T(r)}{r} c_{lm} \frac{dP_{lm}}{d\theta} e^{im\phi} \hat{\boldsymbol{\phi}}. \end{aligned} \quad (10)$$

The sums  $\sum_{lm}$  run from mode  $l = 1$  to  $l = l_{\text{max}}$ , and from order  $m = -l$  to  $m = l$ , where the maximum mode depends on the resolution of the data available.

### 2.2 Vector potential fields

Having determined a general magnetic field expression, next we require the corresponding vector potential field  $\mathbf{A}$ :

$$\mathbf{B} = \nabla \times \mathbf{A}. \quad (11)$$

Given equations (4) and (5), it follows that the poloidal and toroidal components of the vector potential field are

$$\mathbf{A}_{\text{pol}} = \nabla \times (\Phi \hat{\mathbf{r}}), \quad (12)$$

<sup>6</sup>We use a spherical coordinate system where a positive radial field component points towards the observer, the meridional ( $\theta$ ) component is positive pointing from North to South and the azimuthal ( $\phi$ ) component is positive in the clockwise direction as viewed from the North pole.

and

$$\mathbf{A}_{\text{tor}} = \Psi \hat{\mathbf{r}}. \quad (13)$$

Substituting equations (6) and (7) for  $\Phi$  and  $\Psi$  and expanding results in

$$\begin{aligned} \mathbf{A}_{\text{pol}} &= \sum_{lm} \frac{im}{r \sin \theta} S(r) c_{lm} P_{lm} e^{im\phi} \hat{\boldsymbol{\theta}} \\ &- \sum_{lm} \frac{1}{r} S(r) c_{lm} \frac{dP_{lm}}{d\theta} e^{im\phi} \hat{\boldsymbol{\phi}}, \end{aligned} \quad (14)$$

$$\mathbf{A}_{\text{tor}} = \sum_{lm} T(r) c_{lm} P_{lm} e^{im\phi} \hat{\mathbf{r}}. \quad (15)$$

### 2.3 Calculating the helicity density

When expanding equation (3), we find that both  $\mathbf{A}_{\text{pol}} \cdot \mathbf{B}_{\text{pol}}$  and  $\mathbf{A}_{\text{tor}} \cdot \mathbf{B}_{\text{tor}}$  are zero. Consequently, the helicity density equation simplifies to

$$h = \mathbf{A}_{\text{pol}} \cdot \mathbf{B}_{\text{tor}} + \mathbf{A}_{\text{tor}} \cdot \mathbf{B}_{\text{pol}}. \quad (16)$$

By inserting the magnetic field from Section 2.1 (equations 9 and 10) and the vector potential from Section 2.2 (equations 14 and 15), the real part of the magnetic helicity density is given by<sup>7</sup>

$$\begin{aligned} h(r, \theta, \phi) &= \Re \left( \sum_{lm} \sum_{l'm'} \frac{1}{r^2} S(r) T(r) c_{lm} c_{l'm'} e^{i\phi(m+m')} \right. \\ &\times \left. \left( P_{lm} P_{l'm'} \left( l(l+1) - \frac{mm'}{\sin^2 \theta} \right) + \frac{dP_{lm}}{d\theta} \frac{dP_{l'm'}}{d\theta} \right) \right). \end{aligned} \quad (17)$$

As the helicity density is calculated by taking the dot product of sums running between the same limits, the toroidal components have been denoted with a prime in order to distinguish the different sums.

The radial functions  $S(r)$  and  $T(r)$  are the only terms in equation (17) that require information about the specific star considered. Using the ZDI technique (Semel 1989), large-scale magnetic fields can be determined at stellar surfaces ( $r = R_*$ ), which provides values for  $S(R_*)$  and  $T(R_*)$ . Unfortunately, it is unknown how the stellar magnetic field extends beyond this, hence the magnetic helicity density can only be evaluated at the stellar surface.

The surface fields are decomposed into poloidal and toroidal components (e.g. Donati et al. 2006; Vidotto 2016):

$$\begin{aligned} \mathbf{B}_{\text{pol}}(\theta, \phi) &= \sum_{lm} \alpha_{lm} c_{lm} P_{lm} e^{im\phi} \hat{\mathbf{r}} \\ &+ \sum_{lm} \frac{\beta_{lm}}{(l+1)} c_{lm} \frac{dP_{lm}}{d\theta} e^{im\phi} \hat{\boldsymbol{\theta}} \\ &+ \sum_{lm} \frac{\beta_{lm} im}{(l+1) \sin \theta} c_{lm} P_{lm} e^{im\phi} \hat{\boldsymbol{\phi}}, \end{aligned} \quad (18)$$

$$\begin{aligned} \mathbf{B}_{\text{tor}}(\theta, \phi) &= \sum_{lm} \frac{\gamma_{lm} im}{(l+1) \sin \theta} c_{lm} P_{lm} e^{im\phi} \hat{\boldsymbol{\theta}} \\ &- \sum_{lm} \frac{\gamma_{lm}}{(l+1)} c_{lm} \frac{dP_{lm}}{d\theta} e^{im\phi} \hat{\boldsymbol{\phi}}, \end{aligned} \quad (19)$$

<sup>7</sup>The given expression for magnetic helicity density is derived using a left-handed coordinate system, it can be converted to a right-handed coordinate system simply by flipping the sign.

which are characterized by  $\alpha_{lm}$ ,  $\beta_{lm}$ , and  $\gamma_{lm}$  coefficients. A detailed description of how these coefficients are determined given radial, meridional, and azimuthal magnetic field components can be found in Vidotto (2016). Equating this surface field with the full magnetic field (equations 9 and 10) evaluated at  $r = R_*$ ;  $\mathbf{B}(\theta, \phi) = \mathbf{B}(R_*, \theta, \phi)$ , gives

$$S(R_*) = \frac{\alpha_{lm} R_*^2}{l(l+1)}, \quad (20)$$

$$T(R_*) = \frac{\gamma_{lm} R_*}{(l+1)}. \quad (21)$$

Having established expressions for  $S(R_*)$  and  $T(R_*)$ , equation (17) can be evaluated at  $r = R_*$ , which gives the magnetic helicity density at any point  $(\theta, \phi)$  on the stellar surface:

$$h(R_*, \theta, \phi) = \Re \left( \sum_{lm} \sum_{l'm'} \frac{\alpha_{lm} \gamma_{l'm'} R_*}{(l+1)l(l+1)} c_{lm} c_{l'm'} e^{i\phi(m+m')} \right. \\ \left. \times \left( P_{lm} P_{l'm'} \left( l(l+1) - \frac{mm'}{\sin^2 \theta} \right) + \frac{dP_{lm}}{d\theta} \frac{dP_{l'm'}}{d\theta} \right) \right). \quad (22)$$

This expression for helicity density can be applied to any star given only its stellar radius and the  $\alpha_{lm}$  and  $\gamma_{lm}$  coefficients characterizing its poloidal and toroidal magnetic field components.

We note that  $\beta_{lm}$  does not appear in the helicity density equation. This is due to helicity being the linking of toroidal and poloidal fields. The toroidal field lines lie on spherical surfaces, and the poloidal field lines pass through these surfaces. However, only the radial component of the poloidal field links through the toroidal field, the  $\theta$  and  $\phi$  components lie on the same spherical surfaces as the toroidal field and so provide no ‘linkage’. Since the radial part of the poloidal field depends only on  $\alpha_{lm}$ , and the toroidal field depends only on  $\gamma_{lm}$ ,  $\beta_{lm}$  is not needed.

When comparing the helicity density of different stars, or at different times, rather than considering the helicity density at specific points  $(\theta, \phi)$  on the stellar surface, it is more convenient to calculate an average helicity density value across some surface area  $A$ :

$$\langle h \rangle = \frac{\int h(R_*, \theta, \phi) dA}{A}. \quad (23)$$

### 3 APPLICATION

#### 3.1 Observational and simulated data

In this paper, we calculate the large-scale helicity density of the Sun, as well as 51 additional stars listed in Table 1. The magnetic maps we use for each star are referenced in the last column of the table. From left to right, the remaining columns show the name of the star, stellar mass, stellar radius, rotation period, Rossby number, age, absolute helicity density ( $l \leq 4$ ) averaged across the visible stellar hemisphere, the maximum  $l$  mode and the number of magnetic maps used. For references to the stellar parameters listed, as well as a more detailed table with further information on these stars (see Vidotto et al. 2014). The stellar sample consists of stars with spectral types F, G, K, and M, with masses ranging from 0.1 to 1.34  $M_\odot$ . The resolutions of the magnetic maps of the stellar sample range from  $l_{\max} = 4$  to 25, with higher modes indicating a higher resolution, meaning smaller scale magnetic fields are detected. The stars with  $l_{\max} < 8$ , which comprise the majority of the M-dwarfs and hot Jupiter hosts in Table 1, will be omitted for part of the analysis in

Section 3.3 where we choose to consider stars with  $l_{\max} = 8$  to allow for a larger range of  $l$ -modes.

In order to place the Sun in context, we include it in our study. The solar magnetic maps we use come from observations taken by the Helioseismic and Magnetic Imager (HMI) on board the Solar Dynamic Observatory (Pesnell, Thompson & Chamberlin 2012; Scherrer et al. 2012). We also use surface magnetograms taken from the 3D non-potential magnetic field simulation presented in Yeates & Mackay (2012). Together the data spans almost two whole solar cycles; the observed solar data covers most of solar cycle 24, and the simulation is over solar cycle 23. There is a slight overlap in time between the two data sets, which proves useful when checking for consistency between the simulated and observed data. The ability to follow variations in helicity density through a cycle may provide insights into the sources of the scatter in stellar values.

Throughout Section 3.2 the solar helicity will be calculated up to  $l = 8$  only, as this is a reasonable resolution for most of the other stars in our sample. Both the observed and simulated Sun can be recovered to a higher  $l_{\max}$ , but this large-scale helicity density is a reasonable approximation of what we would detect if we could observe the Sun as a star. Only the helicity captured on the largest scales is shown – the contribution from smaller scale features such as active regions is omitted. For the sake of consistency, we compare the stellar and solar data using the same number of  $l$  modes. The lowest resolution used will be  $l \leq 4$ , as this is the highest common mode of the stellar sample in Table 1.

#### 3.2 Large-scale solar helicity densities

We calculate the longitudinally averaged helicity density for every observed and simulated magnetic map and plot it as a function of time in Fig. 1. We use Gaussian smoothing to remove small variations and highlight the overall trends. The helicity densities in the plots are limited to  $\pm 4 \times 10^{12} \text{ Mx}^2 \text{ cm}^{-3}$  (left-hand panel) and  $\pm 4 \times 10^{11} \text{ Mx}^2 \text{ cm}^{-3}$  (right-hand panel) which results in saturation, but reveals more structure towards the equator. The resulting pattern is consistent with the large-scale magnetic helicity density presented by Pipin et al. (2019) in their paper exploring the evolution of the solar magnetic helicity density throughout solar cycle 24 (see their Fig. 5a). Our plot has the opposite polarity to theirs, which may be due to differing sign conventions; using a different coordinate system can change the sign of the helicity density.

The helicity density at the poles of the simulated Sun is approximately a full order of magnitude stronger than that of the observed Sun. However, apart from the magnitude, the two plots show consistent results and match up nicely in the overlapping year ( $\sim 2010$ – $2011$ ), showing a positive south pole and a negative north pole. In both cases, the strong signal at the poles overshadows most structure around the equator and the sign of the helicity density flips across the equator. The helicity is pre-dominantly negative in the Northern hemisphere and positive in the Southern hemisphere until  $\sim 2014$ , when it reverses. A much shorter sign reversal can also be seen around 2000. It is perhaps worthwhile to note that 2000 and 2014 are the years with the highest sunspot activity during solar cycles 23 and 24, respectively<sup>8</sup>; we cannot confidently state whether this is coincidence or consequence.

Calculating the average helicity density across both hemispheres allows us to compare the two more quantitatively. The top panel

<sup>8</sup>Sunspot data from the World Data Center SILSO, Royal Observatory of Belgium, Brussels.

**Table 1.** Our stellar sample. From left to right the columns show: star name, mass, radius, rotation period, Rossby number, absolute helicity density calculated up to  $l \leq 4$  averaged across the visible hemisphere (a mean value if more than one magnetic map is available),  $l_{\max}$ , number of magnetic maps used and references to those magnetic maps. A more comprehensive table can be found in Vidotto et al. (2014).

Star ID	$M_*$ ( $M_\odot$ )	$R_*$ ( $R_\odot$ )	$P_{\text{rot}}$ (d)	$R_o$	Age (Myr)	$ \langle h \rangle _{l \leq 4}$ ( $\text{Mx}^2 \text{cm}^{-3}$ )	$l_{\max}$	No. of maps	Ref.
<i>Solar-like stars</i>									
HD 3651	0.88	0.88	43.4	1.916	8200	1.938e+11	10	1	1
HD 9986	1.02	1.04	23.0	1.621	4300	7.552e+09	10	1	1
HD 10476	0.82	0.82	16.0	0.576	8700	8.060e+09	10	1	1
HD 20630	1.03	0.95	9.30	0.593	600	3.108e+13	10	1	2
HD 22049	0.86	0.77	10.3	0.366	440	8.056e+11	10	1	3
HD 39587	1.03	1.05	4.83	0.295	500	2.379e+12	10	1	1
HD 56124	1.03	1.01	18.0	1.307	4500	2.889e+11	10	1	1
HD 72905	1	1	5.00	0.272	500	1.634e+13	10	1	1
HD 73350	1.04	0.98	12.3	0.777	510	3.771e+11	10	1	1
HD 75332	1.21	1.24	4.80	>1.105	1800	1.230e+12	15	1	1
HD 78366	1.34	1.03	11.4	>2.781	2500	1.305e+12	10	3	4
HD 101501	0.85	0.9	17.6	0.663	5100	3.267e+12	10	1	1
HD 131156A	0.93	0.84	5.56	0.256	2000	2.539e+13	10	7	5, 6
HD 131156B	0.99	1.07	10.3	0.611	2000	1.302e+13	10	1	1
HD 146233	0.98	1.02	22.7	1.324	4700	9.357e+08	10	1	7
HD 166435	1.04	0.99	3.43	0.259	3800	5.368e+12	10	1	1
HD 175726	1.06	1.06	3.92	0.272	500	2.139e+12	10	1	1
HD 190771	0.96	0.98	8.80	0.453	2700	5.472e+12	10	1	7
HD 201091A	0.66	0.62	34.2	0.786	3600	9.288e+10	10	1	8
HD 206860	1.10	1.04	4.55	0.388	260	3.108e+13	10	1	9
<i>Young Suns</i>									
AB Dor	0.76	0.96	0.5	0.026	120	2.318e+14	25	6	10
BD-16351	0.9	0.83	3.39	–	30	6.257e+13	15	1	11
HII 296	0.8	0.74	2.61	–	130	3.731e+13	15	1	11
HII 739	1.08	1.03	2.7	–	130	1.249e+12	15	1	11
HIP 12545	0.58	0.57	4.83	–	21	5.216e+14	15	1	11
HIP 76768	0.61	0.6	3.64	–	120	4.058e+14	15	1	11
TYC	0.69	0.68	3.75	–	120	4.847e+12	15	1	11
0486-4943-1									
TYC	0.85	0.79	4.71	–	120	4.150e+13	15	1	11
5164-567-1									
TYC	0.54	0.54	3.39	–	21	2.305e+13	15	1	11
6349-0200-1									
TYC	0.65	0.64	5.72	–	21	5.125e+13	15	1	11
6878-0195-1									
<i>Hot Jupiter hosts</i>									
$\tau$ Boo	1.34	1.42	3	>0.732	2500	1.722e+11	8.5	6	12, 13, 14, 15
HD 73256	1.05	0.89	14	0.962	830	3.619e+11	4	1	15
HD 102195	0.87	0.82	12.3	0.473	2400	2.687e+12	4	1	15
HD 130322	0.79	0.83	26.1	0.782	930	1.277e+11	4	1	15
HD 179949	1.21	1.19	7.6	>1.726	2100	6.133e+10	6	1	16
HD 189733	0.82	0.76	12.5	0.403	600	8.669e+12	5	2	17
<i>M dwarf stars</i>									
GJ 569A	0.48	0.43	14.7	<0.288	130	1.807e+14	5	1	18
GJ 410	0.58	0.52	14	<0.267	710	1.532e+14	5	2	18
GJ 182	0.75	0.82	4.35	0.054	21	5.905e+14	8	1	18
GJ 49	0.57	0.51	18.6	<0.352	1200	2.494e+13	5	1	18
GJ 494A	0.59	0.53	2.85	0.092	–	1.644e+14	8	2	18
GJ 388	0.42	0.38	2.24	0.047	–	1.238e+14	8	2	19
EQ Peg A	0.39	0.35	1.06	0.02	–	4.550e+14	4	1	19
EQ Peg B	0.25	0.25	0.4	0.005	–	4.724e+14	8	1	19
GJ 873	0.32	0.3	4.37	0.068	–	8.771e+14	8	2	19
GJ 9520	0.55	0.49	3.4	0.097	–	2.173e+14	8	2	18
V374 Peg	0.28	0.28	0.45	0.006	–	9.861e+13	10	2	20
GJ 1111	0.1	0.11	0.46	0.0059	–	1.533e+13	6	3	21
GJ 1156	0.14	0.16	0.49	0.0081	–	1.076e+13	6	3	21
GJ 1245 B	0.12	0.14	0.71	0.011	–	1.565e+13	4	2	21
WX UMa	0.1	0.12	0.78	0.01	–	1.599e+15	4	2	21

Notes. 1: Petit et al. (in preparation); 2: do Nascimento et al. (2016); 3: Jeffers et al. (2014); 4: Morgenthaler et al. (2011); 5: Morgenthaler et al. (2012); 6: Jeffers et al. (in preparation); 7: Petit et al. (2008); 8: Boro Saikia et al. (2016); 9: Boro Saikia et al. (2015); 10: Donati et al. (2003); 11: Folsom et al. (2016); 12: Catala et al. (2007); 13: Donati et al. (2008a); 14: Fares et al. (2009); 15: Fares et al. (2013); 16: Fares et al. (2012); 17: Fares et al. (2010); 18: Donati et al. (2008b); 19: Morin et al. (2008b); 20: Morin et al. (2008a); 21: Morin et al. (2010).

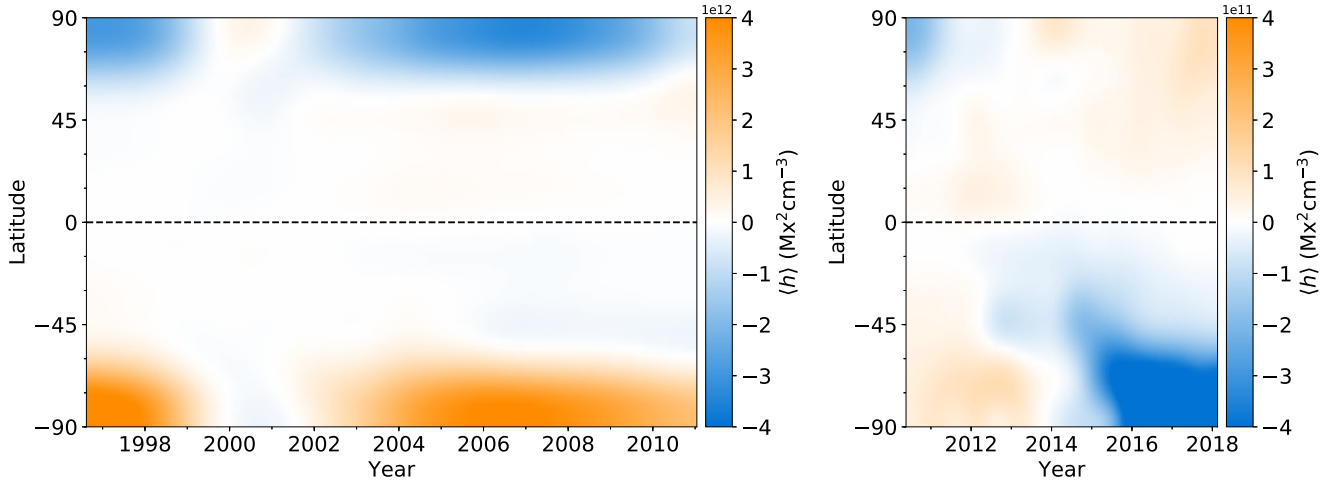


**Figure 1.** The evolution in time of the average solar helicity density for  $l \leq 8$  at each latitude, using simulated data (*left*) and observational data (*right*). Gaussian smoothing has been applied to remove small variations and highlight overall trends. The colour tables saturate at  $\pm 4 \times 10^{12} \text{ Mx}^2\text{cm}^{-3}$  (*left*) and  $\pm 4 \times 10^{11} \text{ Mx}^2\text{cm}^{-3}$  (*right*).

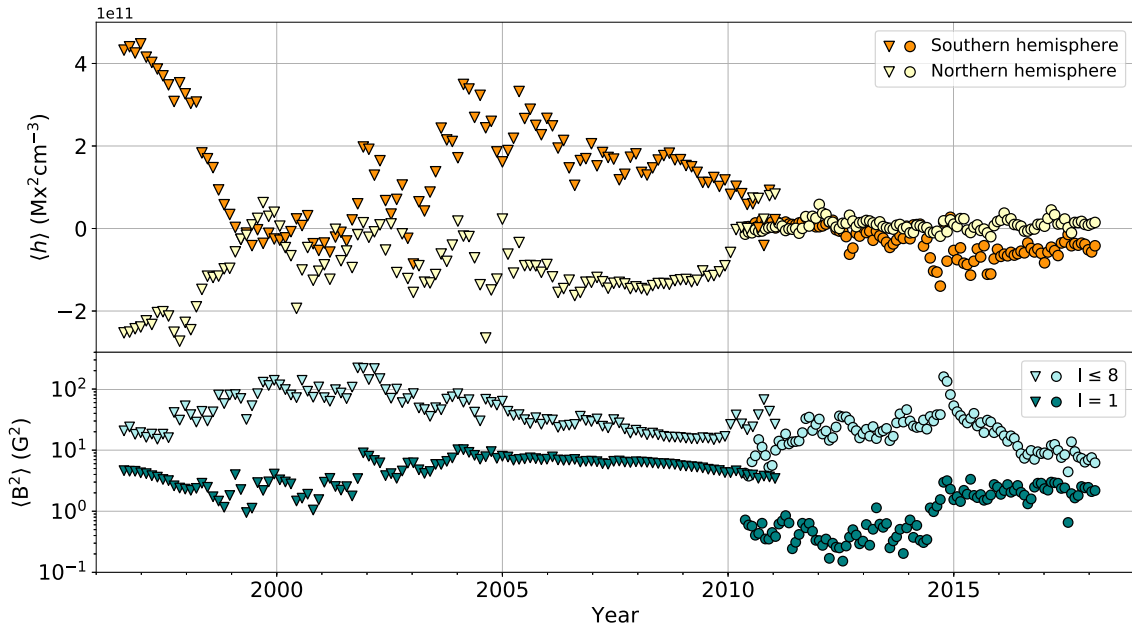


**Figure 2.** *Top:* The evolution in time of the average solar helicity density for  $l \leq 8$  across the Southern (orange) and Northern (yellow) hemispheres. *Bottom:* The mean squared magnetic flux density for  $l \leq 8$  (light teal) and  $l = 1$  (dark teal) across the same time period. The triangles and circles correspond to results based on simulated and observational data respectively.

of Fig. 2 shows the helicity density over time averaged across the Southern (orange) and Northern (yellow) hemispheres, respectively. The triangles correspond to the simulated Sun, and the circles correspond to the HMI observations. Despite having already established that the helicity density flips signs across the equator, this plot reveals more clearly that the overall helicity density of the Sun is never exactly zero. In the case of the simulated Sun, the helicity density is approximately mirrored across the equator, and over time it will average to more or less zero. For the observed Sun on the other hand, the helicity density in the Southern hemisphere dominates throughout the second half of the time period. This could be due to computational errors, or there could be a real imbalance. Yang & Zhang (2012) showed an asymmetry between the large-scale magnetic helicity fluxes in the Northern and Southern hemisphere

across solar cycle 23, which would lead to different amounts of helicity accumulating in each hemisphere. We propose, due to the sign change across the equator, the helicity density averaged across a single hemisphere provides a more meaningful result than an average across the entire sphere, which represents a residual value.

The bottom panel of Fig. 2 shows how the solar magnetic energy for  $l = 1$  and  $l \leq 8$  behaves throughout the same time period over which we are presenting the helicity density in the top panel. The mean squared magnetic flux density across the Sun,  $\langle B^2 \rangle$ , represents a proxy for magnetic energy. The energies of both the simulation and the real Sun follow a similar pattern. On the approach to cycle maximum, the total energy (summed up to mode  $l = 8$ ) increases, while the dipole energy decreases. In the declining phases, as the total energy decreases, the dipole energy first grows, then decreases

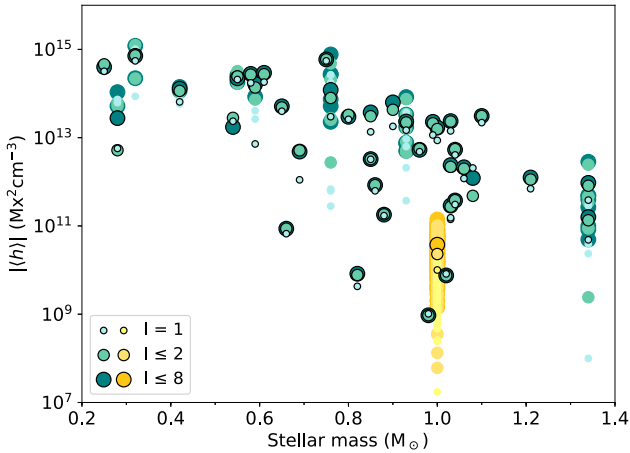


**Figure 3.** Absolute helicity densities averaged across a single hemisphere as a function of stellar mass. The orange shades show the Sun across the Southern hemisphere between  $\sim 2010$  and 2018, and the teal shades show the remaining stars in the stellar sample. The helicity densities are calculated up to different modes, which are represented by different sizes and colours.  $l_{\max}$  increases from small and light to large and dark. Symbols without an outline represent multiple measurements for the same stars, and the symbols with black edges are average values.

slowly to reach another minimum at cycle maximum. The helicity density also follows a cyclic pattern, although shifted later than the total energy by about one quarter in phase.

### 3.3 Large scale stellar helicity densities

Based on the exploration of solar helicity density in the previous section, we choose to compare the helicity densities of our stellar sample in terms of their averages across a single hemisphere. We choose the hemisphere pointing towards the observer, noting that the other is partially obscured, and even partially invisible. Because the sign of the helicity can change across hemispheres or over time, once we have calculated the average we take its absolute value. In the case of the observed solar data, we select the Southern hemisphere. When the Sun is plotted for comparison throughout this section, we are using the observations of the real Sun between  $\sim 2010$  and 2018, not the simulated data.

To explore the importance of the chosen resolution, we plot the absolute average helicity density calculated up to three different  $l$ -mode limits as a function of stellar mass in Fig. 3. The different colours correspond to  $l = 1$  (dipole),  $l \leq 2$  (quadrupole), and  $l \leq 8$ . Consequently, the stars in Table 1 with  $l_{\max} < 8$  are excluded from this plot. The points without black outlines show multiple values for the same star, and the points with black outlines represent average values. An example of this is the Sun, shown in orange shades, where the points with outlines are the average values across  $\sim 2010$ –2018. We find that the helicity densities recovered using dipole or quadrupole fields alone result in good representations of the  $l \leq 8$  helicity density. On average, the  $l = 1$  and  $l \leq 2$  points deviate by  $\sim 40$  and 13 per cent from the  $l \leq 8$  points. Including higher order modes changes the magnitude of the helicity density only slightly, and the general trend across stellar masses remains the same. Hence, for the remainder of this paper we limit ourselves to  $l \leq 4$  in order to increase the number of eligible stars and particularly capture the hot Jupiter hosts and M dwarfs better.

From Fig. 3, we find the absolute helicity density increases with decreasing stellar mass, reaching a plateau for stars of  $M_{\star} \lesssim 0.5 M_{\odot}$ .

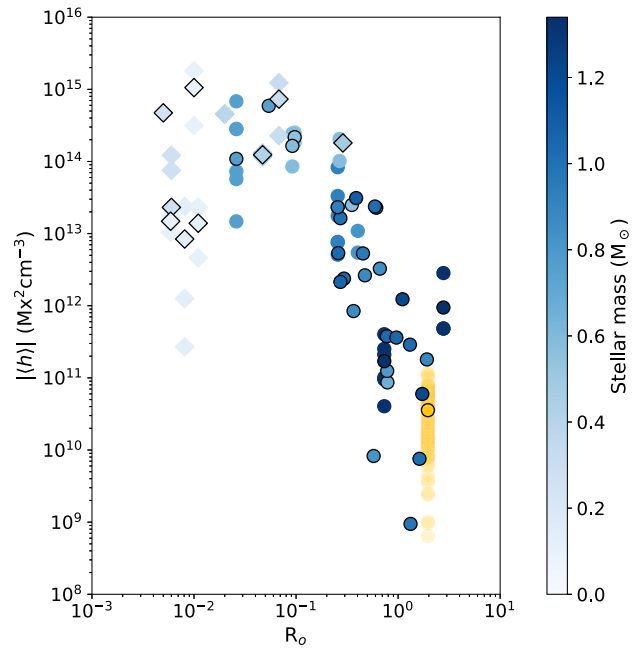


**Figure 4.** Absolute helicity density ( $l \leq 4$ ) averaged across a single hemisphere versus Rossby number. The colour of the symbols correspond to stellar mass, and the diamonds represent stars with  $M_{\star} < 0.5 M_{\odot}$ . Symbols without an outline represent multiple measurements for the same stars, and the symbols with black edges are average values. The orange circles show the range of solar values, for the Southern hemisphere, between  $\sim 2010$  and 2018.

In fact, a number of magnetic field properties have been discovered to change across this  $0.5 M_{\odot}$  boundary (Donati et al. 2008b; Morin et al. 2008b, 2010; See et al. 2015). The authors suggest it is related to the onset of the sharp transition in internal stellar structure from partially convective stars with inner radiative interiors out to  $\sim 0.5 R_{\star}$  (at  $0.5 M_{\odot}$ ) to fully convective stars (at  $0.3 M_{\odot}$ ). As noted by See et al. (2015), there is a correlation between stellar mass and rotation period for our ZDI sample. Generally, the more massive stars in our sample tend to be spinning slower (there are exceptions; we do have some high-mass stars that rotate very fast e.g. AB Dor). This makes it hard to say whether the helicity trend is with mass or rotation. In an attempt to shed light on this, we consider the Rossby number,  $R_0$ ; a parameter that encapsulates information about both mass and rotation period.

Fig. 4 shows the absolute average helicity density versus Rossby number. We use the Rossby numbers listed in Table 1, originally calculated and published in Vidotto et al. (2014). Stars for which we lack Rossby number estimates are omitted from this plot. Stellar mass is denoted by the colour of the symbols. The sample of stars is divided at  $0.5 M_{\odot}$ ; circles represent stars with masses higher than  $0.5 M_{\odot}$  and diamonds represent stars with lower masses. The orange circles show the range of solar values, assuming a solar Rossby number of 1.96 (Cranmer & Saar 2011). As in Fig. 3, the black outlines indicate average values. The helicity density increases, as the Rossby number decreases until a maximum is reached around  $R_0 \sim 0.1$ . Whether this is a true maximum, or simply a saturation is not clear. The same behaviour and saturation point has been reported for other stellar properties such as the ratio of X-ray to bolometric luminosities (Wright et al. 2011) and the toroidal and poloidal magnetic energy densities (See et al. 2015). The stars with masses below  $0.5 M_{\odot}$  are all grouped together in the saturated region, alongside one higher mass, rapidly rotating star at  $R_0 = 0.026$  (AB Dor).

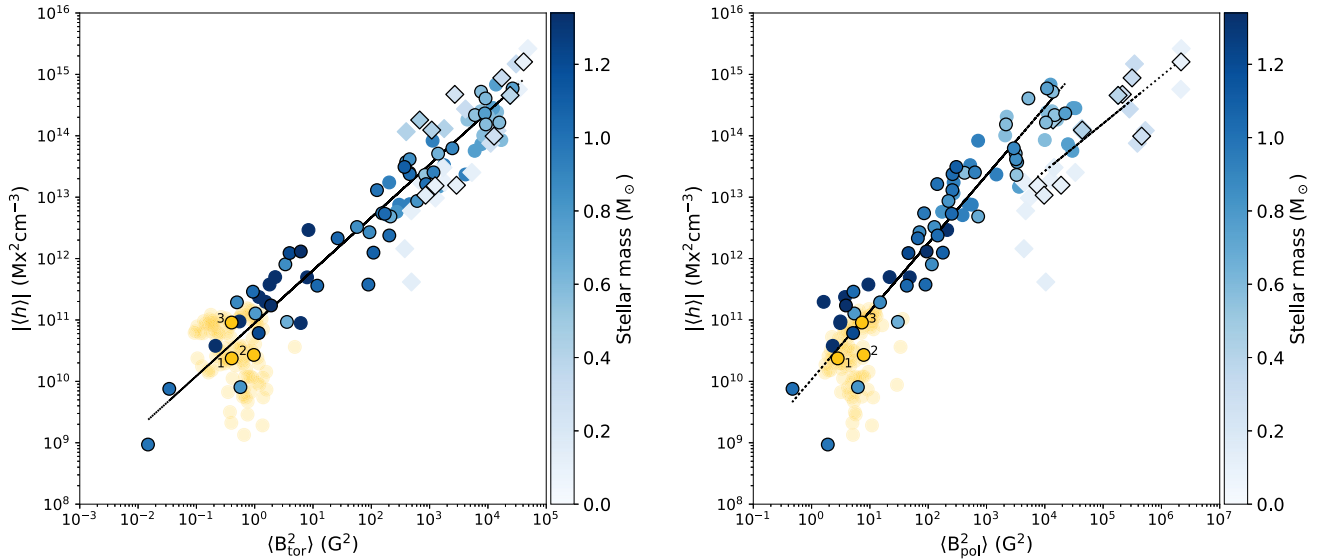


**Figure 5.** Absolute helicity density for  $l \leq 4$  averaged across a single hemisphere versus the mean squared toroidal (*left*) and poloidal (*right*) magnetic flux densities across the star. The symbols are the same as in Fig. 4. Mean values of the solar data are given for the periods  $\sim 2010$ –2012, 2012–2015, and 2015–2018, labelled 1, 2, and 3, respectively. The dashed lines show the best fit of  $|\langle h \rangle| \propto \langle B^2 \rangle^\alpha$  calculated using the average values only. In the toroidal case, one fit is given for all the stars, which results in  $\alpha = 0.86 \pm 0.04$ . In the poloidal case, using all stars would produce a similar value of  $\alpha = 0.85 \pm 0.06$ , but every star with  $M_* < 0.5 M_\odot$  would fall below the line and the overall fit would not be as tight. Consequently, best-fitting lines of stars with  $M_* < 0.5 M_\odot$  and  $M_* > 0.5 M_\odot$  are shown separately, resulting in  $\alpha = 0.77 \pm 0.18$  and  $\alpha = 1.11 \pm 0.07$ , respectively.

See et al. (2015) found that the toroidal magnetic energy density increases faster with Rossby number than the poloidal magnetic energy density. We therefore plot the absolute average helicity density separately against toroidal and poloidal magnetic energy (see Fig. 5). Again the mean squared magnetic flux density across the star,  $\langle B^2 \rangle$ , acts as a proxy for magnetic energy. The shades of blue correspond to stellar mass, and the diamonds indicate stars with  $M_* < 0.5 M_\odot$ . The symbols without an outline represent multiple measurements of the same star, and the symbols with a black outline are average values. Values for the Sun spanning  $\sim 2010$ –2018 are shown in orange, with the circles labelled 1, 2, and 3 being mean values for the periods  $\sim 2010$ –2012, 2013–2015, and 2015–2018, denoting approximately the rising, maximum and declining phases of the cycle. These points show broadly how the Sun’s position on the plot evolves in time. It is notable that the solar cyclic variation is within the scatter in values for other stars.

We find that when the helicity density is plotted against the toroidal magnetic energy; all stars follow the relation  $|\langle h \rangle| \propto \langle B_{\text{tor}}^2 \rangle^{0.86 \pm 0.04}$  regardless of their interior structure. In contrast, when helicity density is plotted against the poloidal magnetic energy, there is a much larger scatter, and the low-mass (largely convective) stars appear to lie on a different slope to those that have a radiative interior.

The evolution with time of the solar field appears to be different for the poloidal and toroidal components. The toroidal field moves from one side to the other of the best-fitting line, whereas the poloidal field mainly stays to the right of the best-fitting line. This can be understood by considering the variation of the large-scale poloidal and toroidal fields plotted against time in Fig. 6. The two components are shown to vary together, but out of phase.

As stellar age is known to affect the magnetic properties of stars we plot the absolute average helicity density against age in Fig. 7. We use the ages listed in Table 1, more information and references for these can be found in Vidotto et al. (2014). We lack ages for some of the M dwarfs in our sample; hence, these are omitted from

the plot. Despite a large spread of values, the figure shows a clear decline in helicity density with age. Given the correlation outlined earlier between helicity density and magnetic field strength, this result reflects the decline of field strength with age.

## 4 DISCUSSION

By truncating our spherical harmonic expansion of the solar magnetic field at low  $l$  values we have explored the variation in the solar helicity density that could be detected if the Sun were observed as a star. While this does not give us a complete picture of the Sun’s helicity density, it allows us to determine the imprint left on the largest scales of the cyclic growth and decay in the solar helicity. This also provides a context within which to view the values we measure for other stars.

Fig. 3 demonstrates clearly the rise in helicity density with decreasing mass that would be expected in light of the high-field strengths of many of the lowest mass stars (Donati et al. 2008b; Morin et al. 2008b, 2010; See et al. 2015). At first glance, the Sun appears to show an anomalously low-helicity density for its mass. Showing the variation with Rossby number instead (Fig. 4) clarifies this however. The Sun is simply a slower rotator than many other stars in our sample of similar mass. Its variation through its cycle is entirely within the scatter of the other stars. What is perhaps more intriguing about this figure, however, is the possible existence of a peak in the helicity density at around  $R_o \approx 0.1$ . This may of course be a plateau, rather than a peak. It is possible that the apparent maximum is a manifestation of bi-stability within the dynamo, leading to two possible regimes; one of weak field and one of strong field (Morin et al. 2011). Further observations are required to confirm this. Several other activity indicators also appear to peak in this parameter range. Super-saturation in X-ray emission (James et al. 2000) has already been suggested for G and K dwarfs, although its existence in M dwarfs is not confirmed (Jeffries et al. 2011; Wright et al. 2011) and more recently the

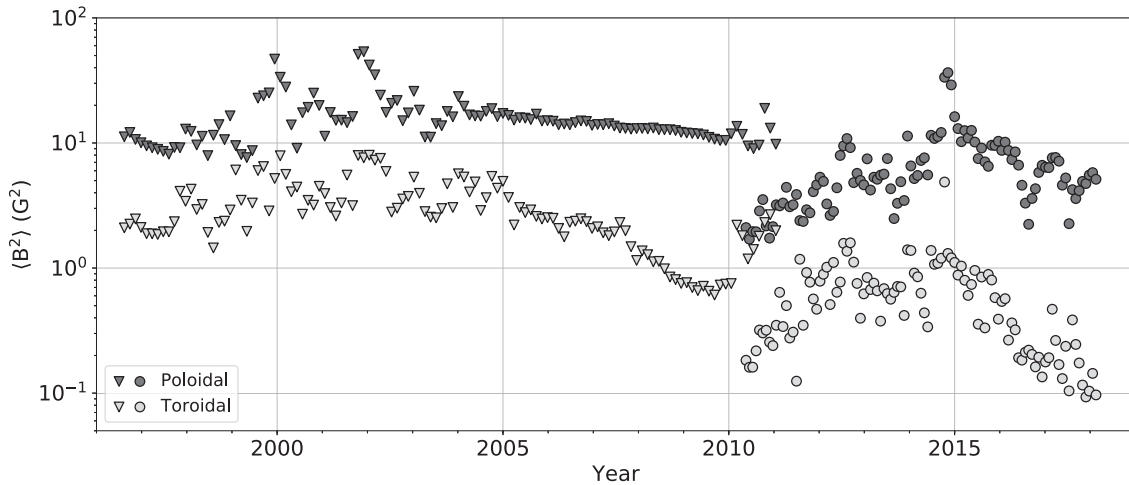


**Figure 6.** The mean squared magnetic flux density ( $l \leq 4$ ) of the poloidal (dark grey) and toroidal (light grey) magnetic field components through the solar cycle. The triangles and circles correspond to results based on simulated and observational data, respectively.

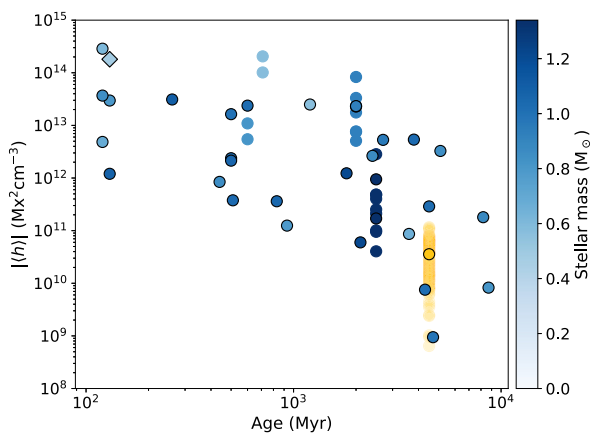


**Figure 7.** Absolute helicity density ( $l \leq 4$ ) averaged across a single hemisphere versus stellar age. Symbols are the same as in Fig. 4.

possibility of a peak in the rate of large M-dwarf flares at  $R_o \approx 0.1$  has been suggested (Mondrik et al. 2019). This is also the regime in which See et al. (2017) find the maximum mass and angular momentum loss rates. This may mark a transition in the geometry of the magnetic fields with some of the lowest Rossby number stars lying in the ‘bi-stable’ regime (Morin et al. 2011; Schrunner, Petitdemange & Dormy 2012; Gastine et al. 2013), where stars with similar parameters may exhibit either strong, simple fields, or weaker, more complex ones. A cyclic variation between these two states has also been proposed (Kitchatinov, Moss & Sokoloff 2014).

Fig. 5 shows a very tight correlation between the large-scale helicity density and toroidal energy density. Since helicity measures the linkage of the poloidal and toroidal fields, this suggests that a common process governs the field geometry of stars in the mass range of  $0.1\text{--}1.34 M_\odot$ , despite their different internal structures and possibly different dynamos. In contrast, plotting helicity density against poloidal energy density appears to separate stars into two families. At a given helicity density, the stars with mass below  $0.5 M_\odot$  appear to have excess poloidal energy density. Is it possible that they have an excess of poloidal field that does not link with the toroidal field and so does not contribute to the helicity? Alternatively, as the differential rotation rate is very low for these

stars, they might be covered with randomly oriented small-scale fields that are not organized at large scales. Such small-scale fields would not contribute to the helicity, but might explain the excess of poloidal field. In order to answer these questions, we would need to map the variation in the fields of the lowest mass stars through their cycles, but this has not yet been done. Indeed, it is not yet clear on what time-scale these stars may show cycles, if at all.

Given the apparent link between energetic and eruptive phenomena on the Sun with its magnetic helicity, it is interesting to see the decline in helicity density with age (Fig. 7). This suggests active phenomena in stars may decline in time. Unfortunately, as we do not have ages for the lowest mass stars in our sample, we cannot investigate the possible role of bifurcation.

## 5 SUMMARY AND CONCLUSIONS

In this paper, we have derived a general expression for calculating the magnetic helicity density of any star given its poloidal and toroidal magnetic field components and radius. Subsequently, we presented solar helicity densities along with the first helicity densities at the surfaces of 51 stars other than the Sun. Our main results are as follows, and all refer to the absolute average helicity density across the visible hemisphere only:

- (i) The helicity density rises and reaches a plateau with decreasing stellar mass. The saturation occurs at  $\sim 0.5 M_\odot$ . This is the result of the corresponding variation of the toroidal field.
- (ii) The helicity density rises with decreasing Rossby number  $R_o$  and reaches a maximum at  $R_o \sim 0.1$ . At lower Rossby numbers, there is some evidence of a subsequent decrease.
- (iii) For our mass range of  $0.1\text{--}1.34 M_\odot$ , the helicity density relates to the toroidal magnetic energy density according to  $|h| \propto \langle B_{\text{tor}}^2 \rangle^{0.86 \pm 0.04}$  with a scatter consistent with the Sun’s variation through its cycle.
- (iv) The variation of the helicity density with the poloidal energy density separates the lower- and higher-mass stars into two families indicated by different slopes similar to the results of See et al. (2015).
- (v) There is an overall decay of helicity density with age.

We conclude that the helicity density of stars with masses lower or higher than  $0.5 M_\odot$  are different if plotted against stellar mass,

Rossby number, or poloidal magnetic energy. The fact that the helicity density of a star of any mass can be determined by the strength of its toroidal magnetic field shows us that the change in behaviour for low-mass stars is due to their relatively strong poloidal fields (See et al. 2015).

When comparing our stars to the Sun we find that, in terms of helicity density, the Sun appears to be a normal example of a star of its mass. Consequently, we suspect the spread in stellar helicity values (for  $M_* > 0.5 M_\odot$ ) may be due to other stars undergoing cycles similar to the Sun, with their helicity density varying in time. We note however that Lehmann et al. (2019) showed a spread in values due to different stellar inclination angles, which may contribute to the scatter in stellar helicity values. In the future, given magnetic maps of the same star over a longer time period, we will investigate how its stellar helicity density evolves in time, compared to the solar case.

## ACKNOWLEDGEMENTS

The authors thank the referee, Prof Mitch Berger, for helpful comments. KL acknowledges financial support from the Carnegie Trust. MJ acknowledges support from STFC consolidated grant no. ST/R000824/1. LTL acknowledges support from the Scottish Universities Physics Alliance (SUPA) prize studentship and the University of St Andrews Higgs studentship. DHM would like to thank both the UK STFC and the ERC (Synergy grant: WHOLE Sun, grant agreement no. 810218) for financial support. VS acknowledges funding from the European Research Council (ERC) under the European Unions Horizon 2020 research and innovation programme (grant agreement no. 682393, AWESoMeStars). JFD and AAV acknowledge funding from the European Research Council (ERC) under the H2020 research and innovation programme (grant agreement nos. 740651, NewWorlds, and 817540, ASTROFLOW).

## REFERENCES

- Berger M. A., 1985, *ApJS*, 59, 433  
 Berger M. A., Field G. B., 1984, *J. Fluid Mech.*, 147, 133  
 Berger M. A., Hornig G., 2018, *JPhA*, 51, 495501  
 Berger M. A., Ruzmaikin A., 2000, *J. Geophys. Res.*, 105, 10481  
 Blackman E. G., 2015, *Space Sci. Rev.*, 188, 59  
 Bonanno A., 2016, *ApJ*, 833, L22  
 Boro Saikia S., Jeffers S. V., Petit P., Marsden S., Morin J., Folsom C. P., 2015, *A&A*, 573, A17  
 Boro Saikia S. et al., 2016, *A&A*, 594, A29  
 Brandenburg A., Subramanian K., 2005, *Phys. Rep.*, 417, 1  
 Catala C., Donati J.-F., Shkolnik E., Bohlender D., Alecian E., 2007, *MNRAS*, 374, L42  
 Chandrasekhar S., 1961, *Hydrodynamic and Hydromagnetic Stability*. Clarendon Press, Oxford  
 Chatterjee P., Guerrero G., Brandenburg A., 2011, *A&A*, 525, A5  
 Cranmer S. R., Saar S. H., 2011, *ApJ*, 741, 54  
 Démoulin P., 2007, *Adv. Space Res.*, 39, 1674  
 Démoulin P., Pariat E., 2009, *Adv. Space Res.*, 43, 1013  
 do Nascimento J.-D. et al., 2016, *ApJ*, 820, L15  
 Donati J.-F., Landstreet J. D., 2009, *ARA&A*, 47, 333  
 Donati J. F. et al., 2008c, *MNRAS*, 390, 545  
 Donati J.-F. et al., 2003, *MNRAS*, 345, 1145  
 Donati J.-F. et al., 2006, *MNRAS*, 370, 629  
 Donati J.-F. et al., 2008a, *MNRAS*, 385, 1179  
 Donati J.-F. et al., 2008b, *MNRAS*, 390, 545  
 Donati J.-F. et al., 2011, *MNRAS*, 417, 1747  
 Fares R. et al., 2009, *MNRAS*, 398, 1383  
 Fares R. et al., 2010, *MNRAS*, 406, 409  
 Fares R. et al., 2012, *MNRAS*, 423, 1006  
 Fares R., Moutou C., Donati J.-F., Catala C., Shkolnik E. L., Jardine M. M., Cameron A. C., Deleuil M., 2013, *MNRAS*, 435, 1451  
 Folsom C. P. et al., 2016, *MNRAS*, 457, 580  
 Gastine T., Morin J., Duarte L., Reiners A., Christensen U. R., Wicht J., 2013, *A&A*, 549, L5  
 Gregory S. G., Donati J.-F., Morin J., Hussain G. A. J., Mayne N. J., Hillenbrand L. A., Jardine M., 2012, *ApJ*, 755, 97  
 Hawkes G., Berger M. A., 2018, in Foullon C., Malandraki O. E., eds, *Proc. IAU Symp. 335, Space Weather of the Heliosphere: Processes and Forecasts*, Cambridge Univ. Press, Cambridge. p. 20  
 James D. J., Jardine M. M., Jeffries R. D., Randich S., Collier Cameron A., Ferreira M., 2000, *MNRAS*, 318, 1217  
 Jeffers S. V., Petit P., Marsden S. C., Morin J., Donati J.-F., Folsom C. P., 2014, *A&A*, 569, A79  
 Jeffries R. D., Jackson R. J., Briggs K. R., Evans P. A., Pye J. P., 2011, *MNRAS*, 411, 2099  
 Kitchatinov L. L., Moss D., Sokoloff D., 2014, *MNRAS*, 442, L1  
 Kochukhov O., Shulyak D., 2019, *ApJ*, 873, 69  
 Lehmann L. T., Hussain G. A. J., Jardine M. M., Mackay D. H., Vidotto A. A., 2019, *MNRAS*, 483, 5246  
 Mondrik N., Newton E., Charbonneau D., Irwin J., 2019, *ApJ*, 870, 10  
 Morgenthaler A., Petit P., Morin J., Aurière M., Dintrans B., Konstantinova-Antova R., Marsden S., 2011, *Astron. Nachr.*, 332, 866  
 Morgenthaler A. et al., 2012, *A&A*, 540, A138  
 Morin J. et al., 2008a, *MNRAS*, 384, 77  
 Morin J. et al., 2008b, *MNRAS*, 390, 567  
 Morin J., Donati J.-F., Petit P., Delfosse X., Forveille T., Jardine M. M., 2010, *MNRAS*, 407, 2269  
 Morin J., Dormy E., Schrunner M., Donati J.-F., 2011, *MNRAS*, 418, L133  
 Nindos A., 2013, in Kosovichev A. G., de Gouveia Dal Pino E., Yan Y., eds, *Proc. IAU Symp. 294, Solar and Astrophysical Dynamos and Magnetic Activity*, Cambridge Univ. Press, Cambridge. p. 519  
 Pariat E., Leake J. E., Valori G., Linton M. G., Zuccarello F. P., Dalmasse K., 2017, *A&A*, 601, A125  
 Pesnell W. D., Thompson B. J., Chamberlin P. C., 2012, *Sol. Phys.*, 275, 3  
 Petit P. et al., 2008, *MNRAS*, 388, 80  
 Pipin V. V., Pevtsov A. A., Liu Y., Kosovichev A. G., 2019, *ApJ*, 877, L36  
 Reiners A., Basri G., 2009, *A&A*, 496, 787  
 Rust D. M., 1994, *Geophys. Res. Lett.*, 21, 241  
 Scherrer P. H. et al., 2012, *Sol. Phys.*, 275, 207  
 Schrunner M., Petitdemange L., Dormy E., 2012, *ApJ*, 752, 121  
 See V. et al., 2015, *MNRAS*, 453, 4301  
 See V. et al., 2017, *MNRAS*, 466, 1542  
 See V. et al., 2019, *ApJ*, 876, 118  
 Semel M., 1989, *A&A*, 225, 456  
 Taylor J. B., 1974, *Phys. Rev. Lett.*, 33, 1139  
 Vidotto A. A., 2016, *MNRAS*, 459, 1533  
 Vidotto A. A. et al., 2014, *MNRAS*, 441, 2361  
 Warnecke J., Peter H., 2019, *A&A*, preprint (arXiv:1910.06896)  
 Woltjer L., 1958, *PNAS*, 44, 489  
 Wright N. J., Drake J. J., Mamajek E. E., Henry G. W., 2011, *ApJ*, 743, 48  
 Yang S., Zhang H., 2012, *ApJ*, 758, 61  
 Yeates A. R., Mackay D. H., 2012, *ApJ*, 753, L34  
 Zhang M., 2013, in Kosovichev A. G., de Gouveia Dal Pino E., Yan Y., eds, *Proc. IAU Symp. 294, Solar and Astrophysical Dynamos and Magnetic Activity*, Cambridge Univ. Press, Cambridge. p. 505  
 Zhang M., Flyer N., 2008, *ApJ*, 683, 1160  
 Zhang M., Low B. C., 2005, *ARA&A*, 43, 103  
 Zhang M., Flyer N., Low B. C., 2006, *ApJ*, 644, 575  
 Zhang M., Flyer N., Chye Low B., 2012, *ApJ*, 755, 78  
 SILSO, World Data Center, Sunspot Number and Long-term Solar Observations, Royal Observatory of Belgium, on-line Sunspot Number catalogue: <http://www.sidc.be/SILSO/>, 1998-2018

This paper has been typeset from a  $\text{\TeX}/\text{\LaTeX}$  file prepared by the author.